ADVANCED ENGINEERING MATERIALS
www.aem-journal.com

Flexible Hybrid Electronic Material Systems with Programmable Strain Sensing Architectures

*Nicholas C. Sears, John Daniel Berrigan, Philip R. Buskohl, and Ryan L. Harne**

Flexible hybrid electronics empower innovative electrical performance capabilities by maintaining electrical conductivity while undergoing large strains. Soft elastomeric material systems are also of great interest for means to control mechanical properties in ways unachievable by bulk materials. This work uncovers the synergy of flexible hybrid electronics and elastomeric material system concepts that becomes manifest by a strategic integration. Conductive silver microflake ink is applied to an elastomeric matrix composed with geometries that tune local strain distributions via microscopic geometries. The selection of internal beam geometries and placement of conductive ink traces are found to govern the strain transfer to the ink and hence the variation of electrical conductivity. Finite element simulations and experiments confirm the relationship between local constituent stretch and the overall material system conductivity. This relationship is exploited via two embodiments that have significant strain-sensitivity or strain-insensitivity. An extension of the concept reveals how both strain sensitivity and insensitivity may be leveraged by a single multifunctional, conductive material system. These results may motivate future concepts for strain sensors, shock isolators, biological monitoring equipment, and more.

1. Introduction

Advancements in flexible hybrid electronics (FHEs) are on a trajectory to deliver new opportunities for a broad range of applications including human health monitoring,[1–4] energy harvesting,[5–7] energy storage,[8,9] and novel consumer products.[10] By combining large compliance and electrical conductivity in material systems, FHEs may overcome challenges associated with fatigue failure induced by strain of conventional wired electronics.[1,11,12] Graphene has served as one material means to combine strength and conductivity for versatile FHEs,[13,14] while also enabling other functions such as flame-retardance and thermal insulation.[15] Metal flake or particle based inks realize conductive electrical traces composed of copper[16] and gold[17] via modified practices of ink jet printing. Silver based inks may exhibit especially strong conductivity,[18,19] print-ability,[20] and electrical robustness when subjected to strain.[20] For instance, Kohlmeyer et. al.[21] investigate the use of conductive silver microflake inks to create free standing, flexible, composite electrodes desirable for conformal energy storage architectures. Furthermore, the strain sensitivity of conductive silver inks has motivated researchers to consider exploiting the property for sake of quantifying strain applied to the FHEs via a sensing mode.[20,22–24] These recent formulations of metallic flake or particle based inks are beginning to pave the way for FHEs to enable new applications of conformal sensors and to replace rigid wired electronics that may be compromised when under stress.

Although the conductivity and robustness of metallic ink traces has improved through myriad investigations,[16,18–21,25] limited knowledge has been obtained on controlling the conductivity of FHE ink traces through unique deformation modes of the host material system. Conductive metal flake or particle based inks are incorporated into FHE-enabled systems via a substrate upon which they are printed, which is often a polymeric or elastomeric material matrix.[18–21,23,25] Elastomers, in fact, are a recent material of choice toward formulating novel material systems that control mechanical properties,[26–28] tune energy dissipation,[29,30] trap shock energy,[31] and guide elastic waves.[32–36] In many such manifestations, the tunable mechanical and dynamic behaviors are realized by the snap-through response associated with reversible buckling beam-like members.[37]

For these reasons, a unique multifunctionality may be cultivated through an integration of FHE-based conductivity and the adaptive mechanical properties of elastomeric material systems. This study investigates such new realization of flexible hybrid electronic material systems by giving attention to two embodiments of the concept: 1) exploiting internal constituent geometry to maximize strain transfer to the conductive traces for strain sensing in a strain-sensitive material system specimen,

Prof. R. L. Harne, N. C. Sears
Department of Mechanical and Aerospace Engineering
The Ohio State University
Columbus, OH 43210, USA
E-mail: harne.3@osu.edu

Dr. J. D. Berrigan, Dr. P. R. Buskohl
Soft Matter Materials Branch
Materials and Manufacturing Directorate
Air Force Research Laboratory
Wright Patterson Air Force Base
OH 45433, USA

The ORCID identification number(s) for the author(s) of this article can be found under https://doi.org/10.1002/adem.201800499.

DOI: 10.1002/adem.201800499

 © 2018 WILEY-VCH Verlag GmbH & Co. KGaA, Weinheim

and 2) tailoring the internal constituent geometry to minimize strain transfer to the flexible ink traces for near-constant conductivity in a strain-insensitive specimen. In this work, compressive strains are studied as a first look into FHE material systems that may bear load and simultaneously deliver unique electrical functionality.

The constant cross-section geometry of the strain-sensitive specimen, **Figure 1**a, is chosen to study the conductivity change associated with a single, defined event of deformation in a material system constituent composed of the conductive ink trace. The elastic buckling of the beam-like member in Figure 1a may be exploited as a foundation for more complex material system geometries.[38] Figure 1c exemplifies the deformation that is associated with the elastic buckling of the strain-sensitive specimen. For the second embodiment of the concept studied in this research, the cross-section geometry of the strain-insensitive specimen is chosen to study the influence on ink trace conductivity when a more progressive collapse behavior occurs via the hexagonal lattice,[39] Figure 1b. The deformation of the strain-insensitive specimen is shown in Figure 1d, suggesting that the diagonally oriented conductive ink trace undergoes deformations more visually similar to rigid body motion than those attributable to strain. Although qualitatively described with the assistance of Figure 1 in this introduction, the naming convention for the specimens is quantitatively justified in Section 4.1.

This report is organized as follows. In Sections 2 and 3, descriptions of the fabrication, experimental testing, and finite element (FE) modeling of the FHE material system specimens are given. Then in Section 4, following experimental verification of the finite element model, additional experimental, and numerical studies are conducted to explore the integration of the FHE and elastomeric material system principles manifest in the two distinct material systems fashioned here. Principal findings from this research are then consolidated in concluding remarks in Section 5.

2. Specimen Descriptions and Fabrication Methods

The substrate material structure of the specimens is fabricated with a 3D printer (Stratasys Objet260 Connex3) using a Stratasys PolyJet material, Tangoblackplus (FLX980). The conductive ink is made from silver (Ag) microflakes (Inframat Advanced Materials, 47MR-10F) and thermoplastic polyurethane (TPU) elastomer (BASF, 50126177). These materials are dissolved in an N-Methyl-2-pyrrolidone (NMP) solvent (Alfa Aesar, A12260) which evaporates to leave Ag-TPU ink. In this research, Ag microflakes constitute 35% of the conductive ink volume (v%), a value selected so as to achieve a percolating network for this class of Ag-TPU ink.[20] Thus, 35 v% Ag-TPU ink is used in the fabrication of all experimental specimens. Wire leads connected to the Ag-TPU ink traces are used for resistance measurements.

The substrate material structures of the material systems are 3D printed with internal channels, approximately 1.4 mm in diameter, for the wire leads (26 gauge) to be inserted and connected to the Ag-TPU ink, as shown in **Figure 2**a. The internal channels provide a way to minimize local stresses on the wire-ink interface. The reduced local stresses in turn help to minimize contact resistances that result from adhering two different conductive materials together. The specimens are printed with a trough on the front of each specimen into which Ag-TPU ink is injected by syringe. The trough is a half-circle cross-section approximately 0.4 mm in diameter. The ends of the trough terminate in the internal channels made for the wire leads. The latter wire leads are used for resistance measurements. This arrangement is shown in a transparent view of the strain-sensitive constituent structure shown in Figure 2a. Additional Ag-TPU ink is injected into the portion of the internal channels immediately connected to the trough to increase the amount of surface area contact between the ink and wire. Epoxy (Hampton Research HR4-347) is injected inside each internal channel and around the wire where the wire

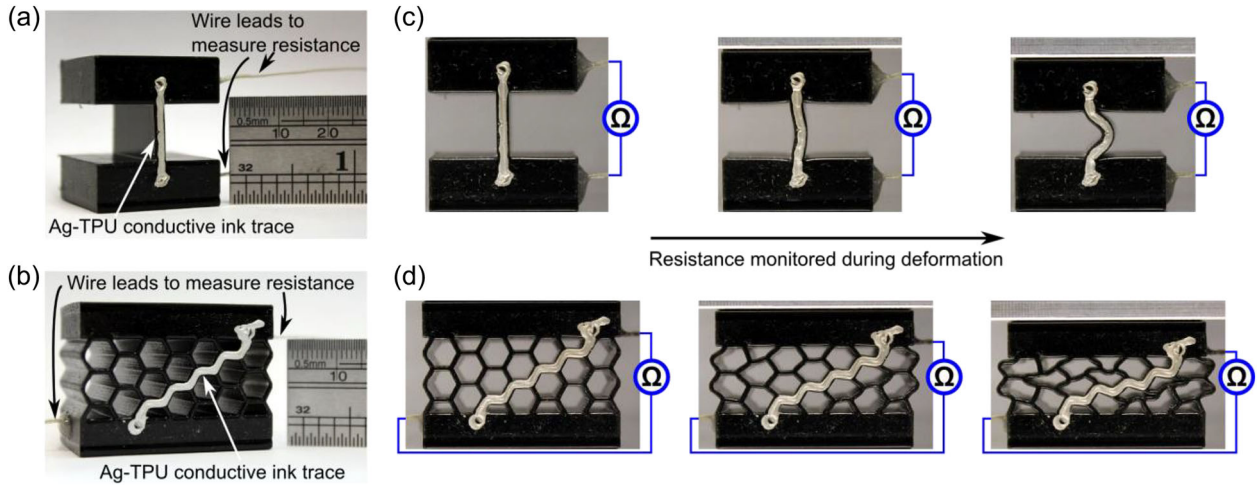

Figure 1. a) Strain-sensitive specimen and b) strain-insensitive specimen with conductive ink traces and wire leads to measure resistance. c) Resistance measured during deformation of strain-sensitive specimen where applied strain results in buckling of vertically oriented conductive ink trace member. d) Resistance measured during deformation of strain-insensitive specimen where conductive ink trace beam undergoes rigid body motion.

© 2018 WILEY-VCH Verlag GmbH & Co. KGaA, Weinheim

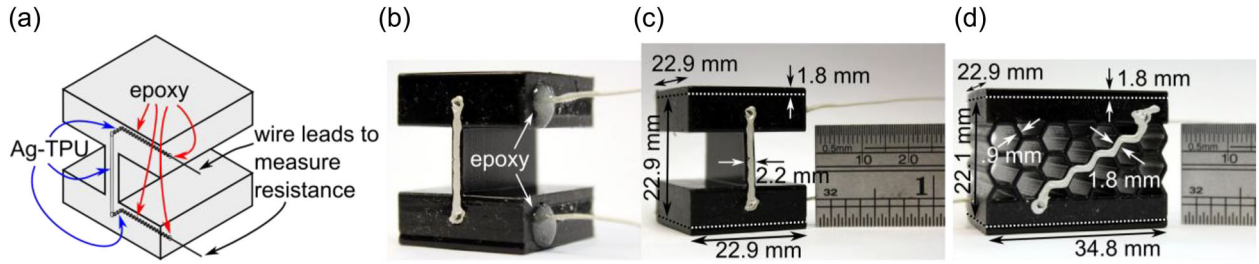

Figure 2. a) Schematic of strain-sensitive specimen with b) epoxy shown around wires on strain-sensitive specimen. Overall dimensions are shown for c) the strain-sensitive specimen and d) the strain-insensitive specimen.

penetrates the specimen, as shown in Figure 2b. The purpose of the epoxy is to stabilize the wire leads at the location of the wire-ink interface, where movement of the wire at the wire-ink interface could enhance resistance values in measurements. Ag-TPU and epoxy application locations are indicated with blue and red, respectively, in Figure 2a. The Ag-TPU ink and epoxy are allowed to fully cure for at least 24 h prior to further use of the specimens.

The strain-sensitive and strain-insensitive specimens have constant cross-section geometries to induce deformation that satisfies plane-strain assumptions when under uniaxial load during experimentation. The dimensions of the strain-sensitive and strain-insensitive specimen are shown in Figure 2c and d, respectively. To aid in 3D printing consistency, 1.8 mm plates made of Veroblackplus (RGD875) are added to the top and bottom of each specimen during the 3D printing process, as shown in Figure 2c and d. With Shore hardness values of 26 (Shore A) and 83 (Shore D) for Tangoblackplus and Veroblackplus, respectively, the 1.8 mm thick plates at the bottom and top of each specimen effectively act as rigid surfaces when the material systems are uniaxially loaded. As a result, the 1.8 mm thick plates of Veroblackplus assist in uniaxial load transfer during mechanical testing. Thus, discounting the 1.8 mm thick plates of Veroblackplus material, the working specimen heights of 22.9 and 22.1 mm for the strain-sensitive and strain-insensitive specimens, respectively, are used for calculation of engineering strain. For the strain-sensitive and strain-insensitive specimens, the material beam member onto which the conductive ink trace is placed is 2.2 and 1.8 mm in thickness, respectively. For the strain-insensitive specimen, the remaining beam members are 0.9 mm in thickness.

3. Experimental Setup and FE Modeling

3.1. Experimental Section

Experimental and FE model results are used to investigate the properties of the multifunctional, conductive, elastomeric specimens. The specimens undergo mechanical properties characterization experiments in a load frame (ADMET eXpert 5600). The uniaxial force applied by the load frame is measured by a load cell (PCB 110205A), while the displacement is monitored by a laser displacement sensor (Micro-Epsilon optoNCDT ILD1700-200). The electrical resistance of the Ag-TPU ink trace is measured in a voltage divider circuit. Data is recorded and processed by a MATLAB program. The experimental setup is illustrated in the schematic shown in **Figure 3**a for reference. Before each experiment, specimens undergo a loading cycle at 3 mm min^{-1} to diminish the Mullin's effect. A loading rate of 0.5 mm min^{-1} is used during data acquisition. The strain-sensitive and strain-insensitive specimens are loaded to peak engineering strains of approximately 19.6% and 16.3%, respectively. The maximum strains are selected to be less than that required to induce self-contact of the specimens in the experiments. The loading and unloading portions of the cycle occur without a pause between.

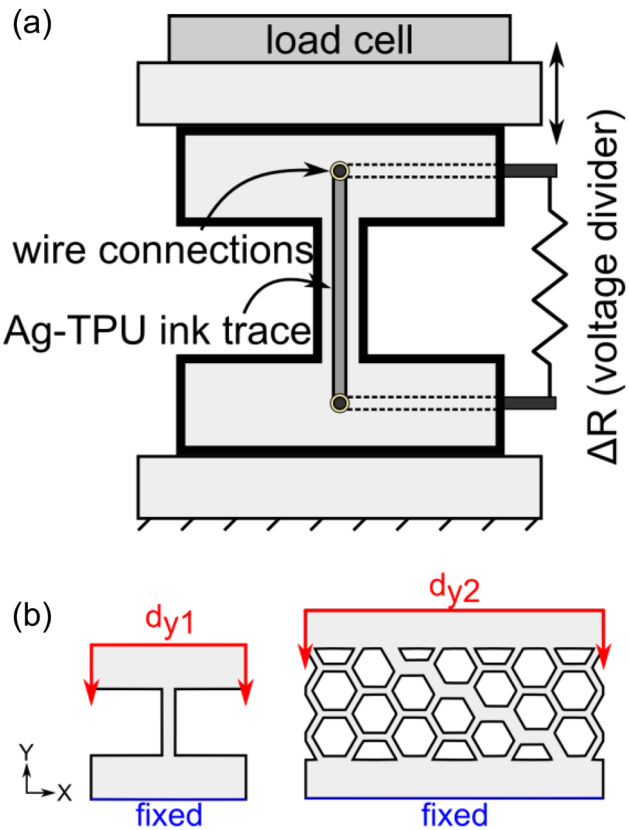

Figure 3. a) Schematic of experimental setup for load frame and resistance evaluations. b) Corresponding FE simulation boundary conditions to emulate experimental method.

© 2018 WILEY-VCH Verlag GmbH & Co. KGaA, Weinheim

3.2. FE Model Formulation

Finite element (FE) models of the specimens are composed by a dynamic implicit formulation in ABAQUS FEA. The dynamic implicit formulation is selected to alleviate concerns associated with a static model to predict large deformation and self-contact events of the specimen deformation when subjected to large applied, engineering strains. The FE models emulate the experimental mechanical properties characterization. A Neo-Hookean, hyperelastic material model is used with the following properties identified for the Tangoblackplus materials: density $\rho = 1112\,\mathrm{kg\,m^{-3}}$, Poisson's ratio $\upsilon = 0.49$, shear modulus $\mu = 248\,\mathrm{kPa}$, and bulk modulus $\kappa = 16.6\,\mathrm{MPa}$. The bottom of each specimen in the respective FE models has fixed displacements and no nodal rotations. As shown in Figure 3b, 2D plane strain models of the specimens are subjected to displacement $d_{y1} = 3.0\,\mathrm{mm}$ and $d_{y2} = 3.5\,\mathrm{mm}$, respectively, linearly ramped over time at a rate of $0.5\,\mathrm{mm\,min^{-1}}$ found to result in sufficiently quasi-static trending behavior for the large applied, engineering strains considered here. Self-contact by tangential friction penalty coefficient of 90% is applied to all edges of the FE model. Additional experiments confirm the plane strain assumption used in the FE model by observing resistance change behavior of ink traces placed on the surface and in the interior of cylindrical specimens of the bulk material (see Supporting Information Section 1). Prior to obtaining final results for processing, a mesh convergence study with CPS4R elements is undertaken to ensure that the FE model outcomes are consistent in quantitative values by a suitably refined mesh.

4. Results and Discussion

4.1. FE Model Validation

Qualitative and quantitative agreements between FE model and experimental results are necessary to confirm the efficacy of the FE model. Specifically, this evaluation is carried out based on the deformation modes and mechanical properties of the specimens under quasi-static loading. **Figure 4**a–d present the experimental and simulation data for the strain-sensitive and strain-insensitive specimens, respectively. For the strain-sensitive and strain-insensitive specimens, the experimental results of measured force to applied, engineering strain respectively shown in Figure 4b and d are provided for one loading cycle that is representative of data obtained from at least three experiments undertaken for at least three nominally identical specimens.

As shown in Figure 4a and c, the deformed strain-sensitive and strain-insensitive specimens in the FE model closely emulate the corresponding deformations observed experimentally. Since the FE model employs a symmetric strain-sensitive material system specimen, the direction of lateral buckling of the vertical beam is associated with the specific mesh generated, and may reverse by the use of a slightly different randomly seeded mesh even if including the same number of elements. The label markers on the deformed shapes in Figure 4a and c correspond to applied, engineering strains with force measurements shown in Figure 4b and d, respectively. Based on the quantitative and qualitative agreement between the FE model predictions and the experimental measurements, it is evident that the FE model is verified for the ability to capture the relevant physics of deformation observed by the conductive elastomeric material system embodiments. On the other hand, deviations are observed between the experiment and FE simulation in Figure 4b for the strain-sensitive specimen after the local maximum of force characteristic of the buckling point. Such deviation may be due to the need for more representative contact formulation in the FE model or may be due to imperfectly known material model that will be explored in future work.

The simulation results in Figure 4a and c are colored according to the maximum principal strain. Recall that the Ag-TPU conductive ink trace on the strain-sensitive specimen in Figure 4a is on the vertical beam member of the cross-section. The large strain on the vertical beam seen in the FE simulation results of Figure 4a suggests that the reversible buckling behavior may have significant influence on the conductivity along the ink trace. Similarly, such large strain may correspond to the elastic energy storage and release associated with the snap-through response.[38] The high principal strain of the conductive ink trace member resulting from the applied uniaxial strain in Figure 4a motivates the naming of the "strain-sensitive"

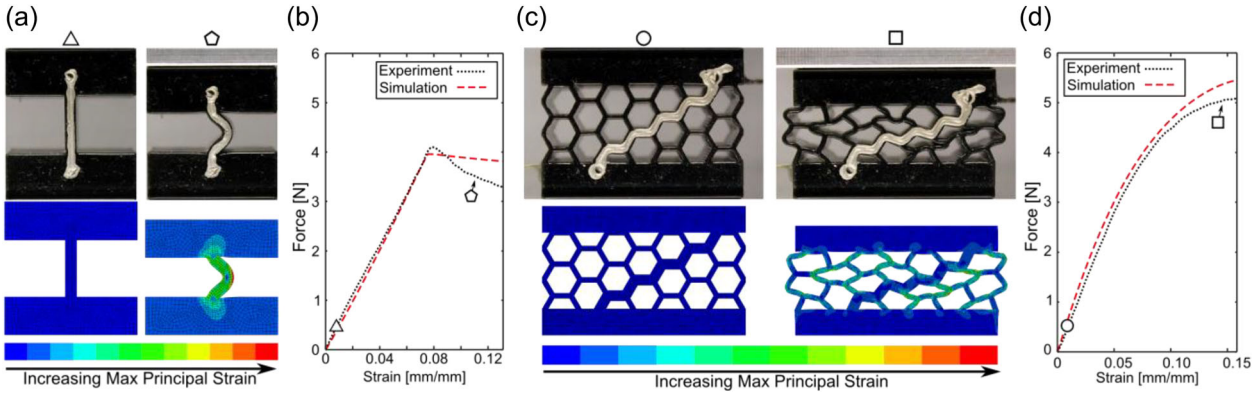

Figure 4. Experimental and FE simulation deformation shapes with force-strain measurements for a and b) strain-sensitive and c and d) strain-insensitive specimens, respectively.

© 2018 WILEY-VCH Verlag GmbH & Co. KGaA, Weinheim

specimen. In contrast, Figure 4c shows that the thicker beam member with conductive ink trace on the strain-insensitive specimen experiences small principal strains when the specimen is subjected to uniaxial engineering strain. Thus, the material system in Figure 4c warrants the name of "strain-sensitive." It remains to be seen how such distinct modes of deformation in the FHE material systems give rise to unique multifunctionality by investigating and capitalizing on the resistance change caused by external applied loads.

4.2. Experimental and FE Model Investigations of the Strain-Sensitive Specimen

To investigate the mechanical and electrical properties of the two concepts of FHE material systems, the specimens undergo displacement cycles in a load frame while the resistances along the conductive ink traces are monitored. The strain-sensitive specimen undergoes a uniaxial displacement cycle with 19.6% peak strain at a loading rate of 0.5 mm min^{-1}. For reference, **Figure 5**a shows the deformation shape of the specimen at pre- and post-buckled states in the loading cycle. The label markers in Figure 5a correspond to those labels shown in Figure 5b and c.

Figure 5b shows the measured force and relative change in resistance of the strain-sensitive specimen according to applied strain for a single loading cycle. The R is the resistance across the conductive ink trace, and ΔR is the difference of measured resistance R and initial resistance R_0. In other words, the relative resistance change shown in Figure 5b is $\Delta R/R_0 = R/R_0 - 1$. As shown in Figure 5b, the force is linearly related to strain until forces approach the maximum force of the loading cycle, which corresponds to the maximum force of the buckling event. Around this maximum force, it is evident that the resistance is near its minimum. The buckling event is followed by a region revealing negative stiffness, during which a decreasing reaction force and increasing and leveling out resistance are observed for a continued increase in uniaxial displacement. After reaching the maximum strain of the loading cycle, the specimen is released at the same displacement rate until the force and strain approach zero. Within the portion of the loading cycle during which the specimen is released, the resistance of the ink trace on the post-buckled beam is shown to decrease until the beam is once again straight, after which the resistance increases. The measured force of the specimen is insightful to exemplify its function as a mechanical metamaterial constituent for temporary energy storage and release. On the other hand, insight into the origin of the resistance changes remains to be uncovered.

The FE model is used to investigate the trends of ink trace resistance change by evaluating the arc length of the conductive ink trace S. Figure 5c shows the change in resistance measured experimentally and the relative change of ink trace arc length $\Delta S/S_0$ computed from FE simulation results. Indeed, these findings show a clear relationship between changes in resistance and changes in ink trace arc length. To explore this qualitatively, Figure 5d presents the absolute values of the relative changes of resistance and arc length normalized to the maxima of their absolute values, respectively denoted by $|\Delta R|/|\Delta R|_{\max}$ and $|\Delta S|/|\Delta S|_{\max}$. These results are also compared to the measured force normalized to maximum force for the same range of strain, $F/F_{\max}$. The maximum force, maximum change in arc length, and minimum resistance are discovered to occur for the same values of strain, which is the elastic buckling point.

In recent work on conductive Ag-TPU ink traces, Valentine et al.[20] establish power law relationships between the conductivity of the ink traces and the concentration of Ag microflakes in the elastic matrix. More specifically, the conductivity of the Ag microflakes in the Ag-TPU composite form a percolating network where the conductivity is governed by the probability that Ag flakes are in contact with adjacent flakes.[40] The dependence of the electrical resistance of the Ag-TPU ink trace on microflake proximity explains why the resistance of the ink trace is sensitive to changes in arc length that arise from the deformation behavior of the strain-sensitive specimen in Figure 5a. For example, in the linear elastic deformation region of Figure 5c prior to the buckling point, the microflakes are compressed, resulting in a decrease in resistance. Beyond this region, Ag microflakes are separated by the increased arc length of the vertical beam member so that resistance increases. Additional experiments confirm this relationship by showing that the change in resistance is

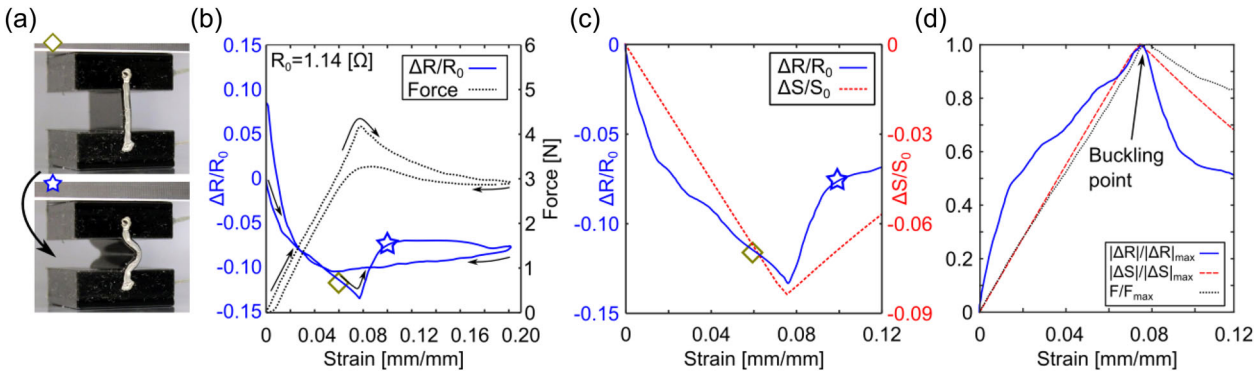

Figure 5. a) Deformation shape of strain-sensitive specimen for reference, b) experimental change in both resistance and force according to strain for a loading cycle with arrows denoting loading and unloading portions, c) experimental change in resistance and FE-predicted change in arc length for a portion of the loading cycle, and d) experimental normalized resistance change, FE-predicted arc length change, and experimental force change according to strain for a portion of the loading cycle.

© 2018 WILEY-VCH Verlag GmbH & Co. KGaA, Weinheim

correlated to arc length strain by the comparison of relative resistance changes for the strain-sensitive specimen and for a solid cube of the bulk material of identical overall dimension with a surface-applied ink trace (see Supporting Information Section 2). These findings suggest that conductive ink traces aligned and integrated with buckling material system constituents can be leveraged within the composition of complex material systems to create a multifunctional, conductive, elastomeric material system network capable of buckling event detection, load characterization, or other functional purposes.

4.3. Experimental and FE Model Investigations of the Strain-Insensitive Specimen

Insights into the sensitivities of the conductive ink trace to strain gained from the strain-sensitive specimen are used to reverse the concept and strategically exploit the conductive ink traces in FHE material systems in ways that may minimize strain transfer to the conductive Ag-TPU ink. A qualitative evaluation of the strain-insensitive specimen deformation in Figure 4c suggests that the unique deformation mode may suppress such strain transfer to the ink trace. **Figure 6**a shows the deformation shape of the strain-insensitive specimen at two locations in the loading cycle. Figure 6b shows the measured force and resistance of the specimen for a cycle of applied strain to 16.3% peak strain at a loading rate of .5 mm min^{-1}. Figure 6b shows that the change in resistance across the Ag-TPU ink trace on the strain-insensitive specimen is negligible throughout the loading cycle. In comparison with the resistance change of the strain-sensitive specimen in Figure 5b that reaches a maximum resistance change of approximately 14%, the conductive ink trace of the strain-insensitive specimen exhibits normalized resistance deviation of 1% at most. Figure 6c further underscores the correlation between relative resistance change and relative arc length change of the conductive ink trace for the strain-insensitive specimen.

Indicated by the small changes in arc length of the ink trace beam shown in Figure 6c, the deformation mechanism of the ink trace beam on the strain-insensitive specimen is more similar to that of rigid body motion than to strain. The particular geometry of the strain-insensitive specimen, as shown in Figure 2d, features a conductive ink trace beam twice as thick as its surrounding counterparts. Additionally, the ink trace beam is not aligned to the direction of applied strain as it is for the strain-sensitive specimen. Therefore, the Ag-TPU ink trace experiences small changes in arc length and resistance that result in a near-constant conductivity.

4.4. Programming the Conductive Ink Network for Strain Sensing

The strain-sensitive and strain-insensitive specimens exemplify that the concept of FHE material systems devised may deliver a breadth of strain sensing functionality. To explore how to exploit such capabilities, a modified strain-insensitive specimen is fabricated with a network of electrical paths. As shown in **Figure 7**a, Ag-TPU ink traces are placed over a selection of the strain-insensitive specimen cross-section geometry. The maximum principal strain profile predicted by the FE model in Figure 3c suggests that the strain transfer to the ink in certain of the new ink trace paths may heighten resistance change observed when the specimen is subjected to applied, engineering strains. In the experiments, resistance is probed from the measurement node to either the primary node or to nodes 1, 2, or 3, as shown in Figure 7a. Thus, four measurements of resistance change are obtained. To accommodate the thinner electrical connections to nodes 1, 2, or 3, the modified strain-insensitive specimen is fabricated with dimensions that are 110% of the size of the original strain-insensitive specimen. Therefore, compared to the path from the measurement to primary node that uses an ink trace path geometry of thickness 2 mm, the ink trace paths following nodes 1, 2, and 3 utilize beam thicknesses of 1 mm. In other words, the deformations over paths ending at nodes 1, 2, and 3 may be more highly strained than along the path from measurement to primary nodes, as exemplified in the FE

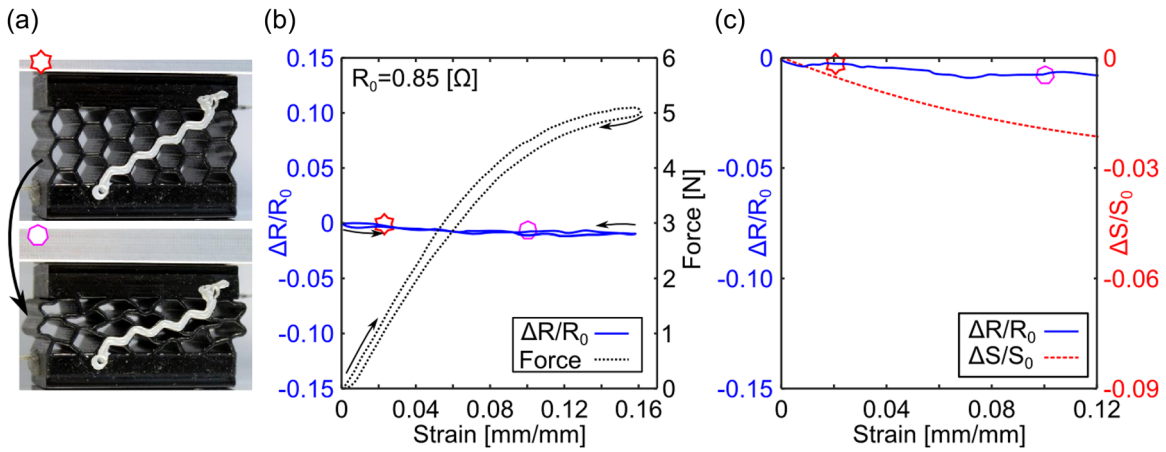

Figure 6. a) Deformation shape of strain-insensitive specimen for reference, b) change in resistance and force according to strain for a loading cycle with arrows denoting loading and unloading portions, and c) change in resistance and arc length for a portion of the loading cycle.

© 2018 WILEY-VCH Verlag GmbH & Co. KGaA, Weinheim

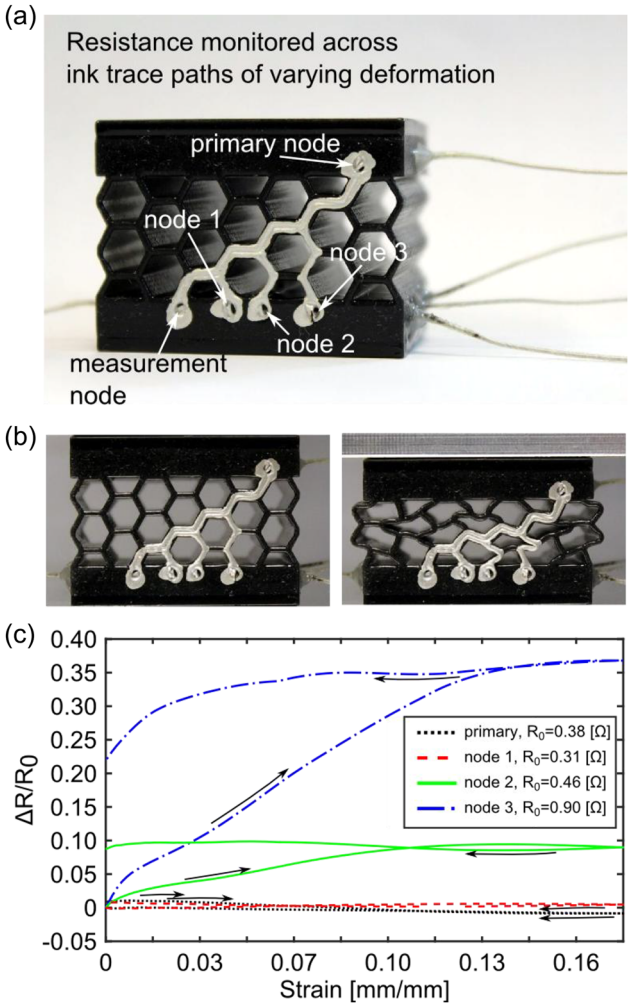

Figure 7. a) Modified strain-insensitive specimen with original ink trace path (primary) and additional ink trace paths determined by resistance measurement location at nodes 1, 2, and 3. b) Under compression, varying degrees of deformation in each ink trace path result in c) corresponding degrees of resistance change observed experimentally.

results of Figure 4c. In the following experiments, a load rate of 5 mm min^{-1} is used in the uniaxial compression cycles.

As verified by the photographs in Figure 7b, the ink traces connecting the measurement node to nodes 1, 2, and 3 deform differently under the uniaxial strain of the specimen. The FE model results of Figure 4c confirm that local strains along the paths terminating in node 3, node 2, node 1, and the primary node decrease in cumulative magnitude respecting each other.

Figure 7c shows the corresponding change in resistance for each of the conductive networks paths for a full cycle of compression to 17.5% peak strain and release. In agreement with the FE predictions of Figure 4c and correlation of local strain change to change in resistance, Figure 7d shows that with increasing uniaxial applied strain to the modified material system, measurements to nodes 1, 2, and 3 show increasing changes in resistance. Exploiting this conductive specimen composition, one could select the preferred network of ink traces to program an extent of strain-sensitivity in the specimen to detect macroscopic deformation of the FHE material system.

The potential applications of this concept span a wide range of practices that may benefit by leveraging soft electronics. For instance, the small changes in resistance of the primary conductive ink trace path in the strain-insensitive specimen may be useful for future applications of electronics protection with a nearly constant electrical resistance. Protective capabilities may be suggested by the low dynamic stiffness observed in Figure 6b as the honeycomb beam geometry of the strain-insensitive specimen is uniaxially loaded. In addition, the large changes in resistance arising from regions of highly localized strain of the ink trace paths connecting to nodes 2 and 3 in the modified strain-sensitive specimen may serve as mechanisms to detect applied loads. Integrated with polymer films, exploiting the FHE and material system principles newly synchronized in this work may inspire concepts for monitoring the motility of such films undergoing autonomous deformations[41] tailored according to unique film-based material system geometries. Indeed, these findings emphasize that the framework of FHE material systems may deliver unique multifunctionality via strain sensing and electronics protection achieved by exploiting relative strain transfer between the deformed constituent geometry and conductive ink traces.

5. Conclusions

In summary, the science of flexible hybrid electronics and elastomeric material systems is advanced in this research via a new foundation for the integration of these concepts in a unique, multifunctional class of conductive material systems. Through experimental and simulation efforts, it is shown that the change in resistance of the conductive ink trace is correlated with the change in arc length and local strain of the ink trace. It is found that ink traces aligned with buckling material system constituents may empower means to detect collapse and elastic energy absorption events. Additionally, it is demonstrated that conductive ink traces placed along paths undergoing minimal changes in arc length and experiencing small local strains can be used to suppress resistance change. This may be advantageous in applications where vibration isolation and data transmission are concurrently required, such as for electronics packaging. Alternatively, a large resistance change can be achieved despite minimal changes in arc length in the presence of highly localized strains. This suggests that a desired resistance response can be programmed through strategic choices in specimen geometry and ink trace path. Overall, the findings suggest that FHEs and elastomeric material systems may be successfully integrated for functionality uniquely manifest at the intersection of concepts by controlling the deformation modes of FHEs for a desired electrical response.

Supporting Information

Supporting Information is available from the Wiley Online Library or from the author.

© 2018 WILEY-VCH Verlag GmbH & Co. KGaA, Weinheim

Acknowledgments

The authors kindly acknowledge James Hardin of UES, Inc. and Jim Deneault of UTC for helpful discussions and advice regarding specimen fabrication. This work is supported by the Air Force Research Laboratory and Dayton Area Graduate/Faculty Fellowship Program via grant number RX1-OSU-17-4.

Conflict of Interest

The authors declare no conflict of interest.

Keywords

collapse and buckling, flexible electronics, soft material systems, strain sensing

Received: May 8, 2018
Published online: June 7, 2018

[1] B. Li, Y. Gao, A. Fontecchio, Y. Visell, *Smart Mater. Struct.* **2016**, *25*, 1.
[2] Y. Khan, M. Garg, Q. Gui, M. Schadt, A. Gaikwad, D. Han, N.A.D. Yamamoto, P. Hart, R. Welte, W. Wilson, S. Czarnecki, M. Poliks, Z. Jin, K. Ghose, F. Egitto, J. Turner, A.C. Arias, *Adv. Funct. Mater.* **2016**, *26*, 8764.
[3] X. Wang, Y. Gu, Z. Xiong, Z. Cui, T. Zhang, *Adv. Mater.* **2014**, *26*, 1336.
[4] A. K. Bansal, S. Hou, O. Kulyk, E. M. Bowman, I. D. W. Samuel, *Adv. Mater.* **2015**, *27*, 7638.
[5] S. Lee, S. Bar, L. Lin, S. Ahn, C. Park, S. Kim, S. N. Cha, Y. J. Park, Z. L. Wang, *Nano-Energy* **2013**, *2*, 817.
[6] Y. Yang, H. Zhang, G. Zhu, S. Lee, Z. Lin, Z. Wang, *Am. Chem. Soc. NANO* **2012**, *7*, 785.
[7] S. Park, H. Kim, M. Vosgueritchian, S. Cheon, H. Kim, J. H. Koo, T. R. Kim, S. Lee, G. Schwartz, H. Chang, Z. Bao, *Adv. Mater.* **2014**, *26*, 7324.
[8] L. Wen, F. Li, H. Cheng, *Adv. Mater.* **2016**, *28*, 4306.
[9] K. Park, J. H. Son, G. Hwang, C. K. Jeong, J. Ryu, M. Koo, I. Choi, S. H. Lee, M. Byun, Z. L. Wang, K. J. Lee, *Adv. Mater.* **2014**, *26*, 2514.
[10] D. Xu, A. Tairych A, I. A. Anderson, *Smart Mater. Struct.* **2016**, *25*, 1.
[11] J. T. Allen, B. P. DeFigueiredo, S. P. Magleby, in *ASME 2017 International Design Engineering Technical Conferences and Computers and Information in Engineering Conference*, Cleveland, Ohio, USA, 2017, DETC2017-68370.
[12] J. A. Rogers, T. Someya, Y. Huang, *Science* **2010**, *327*, 1603.
[13] Y. Haung, Y. Zhao, Y. Wang, X. Guo, Y. Zhang, P. Liu, C. Liu, Y. Zhang, *Smart Mater. Struct.* **2018**, *27*, 1.
[14] H. Jang, Y. J. Park, X. Chen, T. Das, M. Kim, J. Ahn, *Adv. Mater.* **2016**, *28*, 4184.
[15] Q. Zhang, D. Lin, B. Deng, X. Xu, Q. Nian, S. Jin, K. D. Leedy, H. Li, G. J. Cheng, *Adv. Mater.* **2017**, *29*, 1.
[16] S. Jeong, K. Woo, S. Lim, J. S. Kim, H. Shin, Y. Xia, J. Moon, *Adv. Funct. Mater.* **2008**, *18*, 679.
[17] P. Chandra, J. Singh, A. Singh, A. Srivastava, R. N. Goyal, Y. B. Shim, *J. Nanopart.* **2013**, *2013*, 1.
[18] H. Jiang, K. Moon, Y. Li, C. P. Wong, *Chem. Mater.* **2006**, *18*, 2969.
[19] R. Zhang, K. Moon, W. Lin, C. P. Wong, *J. Mater. Chem.* **2010**, *20*, 2018.
[20] A. D. Valentine, T. A. Busbee, J. W. Boley, J. R. Raney, A. Chortos, A. Kotikian, J. D. Berrigan, M. F. Durstock, J. A. Lewis, *Adv. Mater.* **2017**, *29*, 1.
[21] R. R. Kohlmeyer, A. J. Blake, J. O. Hardin, E. A. Carmona, J. Carpena-Nunez, B. Maruyama, J. D. Berrigan, H. Huang, M. F. Durstock, *R. Soc. Chem.* **2016**, *4*, 16856.
[22] S. Khan, L. Lorenzelli, *Smart Mater. Struct.* **2017**, *26*, 1.
[23] S. Merilampi, T. Bjorninen, V. Haukka, P. Ruuskanen, L. Ukkonen, L. Sydanheimo, *Microelectron. Reliab.* **2010**, *50*, 2001.
[24] S. Merilampi, T. Bjorninen, L. Ukkonen, P. Ruuskanen, L. Sydanheimo, *Sens. Rev.* **2011**, *31*, 32.
[25] K. Chun, Y. Oh, J. Rho, J. Ahn, Y. Kim, H. R. Choi, S. Baik, *Nat. Nanotechnol.* **2010**, *5*, 853.
[26] K. Bertoldi, P. M. Reis, S. Willshaw, T. Mullin, *Adv. Mater.* **2010**, *22*, 361.
[27] J. T. B. Overvelde, S. Shan, K. Bertoldi, *Adv. Mater.* **2012**, *2*, 2337.
[28] A. Lazarus, P. M. Reis, *Adv. Eng. Mater.* **2015**, *17*, 815.
[29] J. Bishop, Q. Dai, Y. Song, R. L. Harne, *Adv. Eng. Mater.* **2016**, *18*, 1871.
[30] T. Frenzel, C. Findeisen, M. Kadic, P. Gumbsch, M. Wegener, *Adv. Mater.* **2016**, *28*, 5865.
[31] S. Shan, S. H. Kang, J. R. Raney, P. Wang, L. Fang, F. Candido, J. A. Lewis, K. Bertoldi, *Adv. Mater.* **2015**, *27*, 4296.
[32] R. S. Lakes, T. Lee, A. Bersie, Y. C. Wang, *Nature* **2001**, *410*, 565.
[33] P. Wang, F. Casadei, S. Shan, J. C. Weaver, K. Bertoldi, *Phys. Rev. Lett.* **2014**, *113*, 014301.
[34] D. M. Kochmann, *Mech. Res. Commun.* **2014**, *58*, 36.
[35] S. Shan, S. H. Kang, P. Wang, C. Qu, S. Shian, E. R. Chen, K. Bertoldi, *Adv. Funct. Mater.* **2014**, *24*, 4935.
[36] J. Shim, P. Wang, K. Bertoldi, *Int. J. Solids Struct.* **2015**, *58*, 52.
[37] R. L. Harne, K. W. Wang, *Harnessing Bistable Structural Dynamics For Vibration Control, Energy Harvesting, and Sensing*, John Wiley & Sons Ltd, Chichester **2017**.
[38] N. Hu, R. Burgueño, *Smart Mater. Struct.* **2015**, *24*, 063001.
[39] D. M. Correa, T. Klatt, S. Cortes, M. Haberman, D. Kovar, C. Seepersad, *Rapid Prototyping J.* **2015**, *21*, 193.
[40] D. Stauffer, A. Aharony, *Introduction to Percolation Theory*, 2nd ed., Taylor & Francis, Philadelphia, PA **1994**.
[41] B. E. Treml, R. N. McKenzie, P. Buskohl, D. Wang, M. Kuhn, L. S. Tan, R. A. Vaia, *Adv. Mater.* **2018**, *30*, 1705616.

 © 2018 WILEY-VCH Verlag GmbH & Co. KGaA, Weinheim

Supporting Information

Flexible hybrid electronic material systems with programmable strain sensing architectures

By *Nicholas C. Sears, John Daniel Berrigan, Philip R. Buskohl, and Ryan L. Harne**

Prof. Ryan L. Harne, Mr. Nicholas C. Sears
Department of Mechanical and Aerospace Engineering, The Ohio State University, Columbus, OH 43210, USA
Email: harne.3@osu.edu

Dr. John Daniel Berrigan, Dr. Philip R. Buskohl
Soft Matter Materials Branch, Materials and Manufacturing Directorate, Air Force Research Laboratory, Wright Patterson Air Force Base, OH 45433, USA

1 Evaluation of potential out-of-plane behavior and ink trace trough placement

The FE models employ two-dimensional geometries via plane strain assumptions. Plane strain examinations assume that the strain out of the plane is negligible in comparison to the strain in the plane. To investigate the possibility that out-of-plane deformation occurs so as to influence the strain distribution within the ink trace, and hence influence resistance measurements, additional specimens are fabricated in cylindrical geometries and employed in further experiments. As shown in Figs. S1(a) and (b), an Ag-TPU ink trace trough is placed on the surface and in the center of cylindrical specimens, respectively. The ink trace trough on the surface of the specimen in Fig. S1(a) has a half-circle shape with diameter 0.4 mm. The ink trace trough that travels along the central axis of the other specimen in Fig. S1(b) is a full-circle 0.4 mm in diameter. When these cylindrical specimens are tested in the load frame to an applied compressive displacement of 1.0 mm peak at a rate of 3 mm/min, Fig. S1(c) shows the measured results of normalized resistance change. The cylindrical specimen with the Ag-TPU ink trace trough on the surface reveals

insignificant resistance change. This trend suggests that possible out-of-plane or bulging deformation does not occur so as to influence the resistance data. In contrast, the specimen with the internal ink trough shows large changes in resistance. Due to the toroidal shape due to the central trough along with the applied uniaxial compressive load, the large resistance reduction associated with the loading portion of the cycle is likely related to the contraction of the interior trough wherein the ink trace is applied. This contraction compresses the silver microflakes in the ink so as to enhance conductivity and decrease resistance. Thus, for the strain-sensitive and strain-insensitive specimens used in this research where the ink traces are placed on the specimen surfaces, the plane strain assumptions of the FE model are justified.

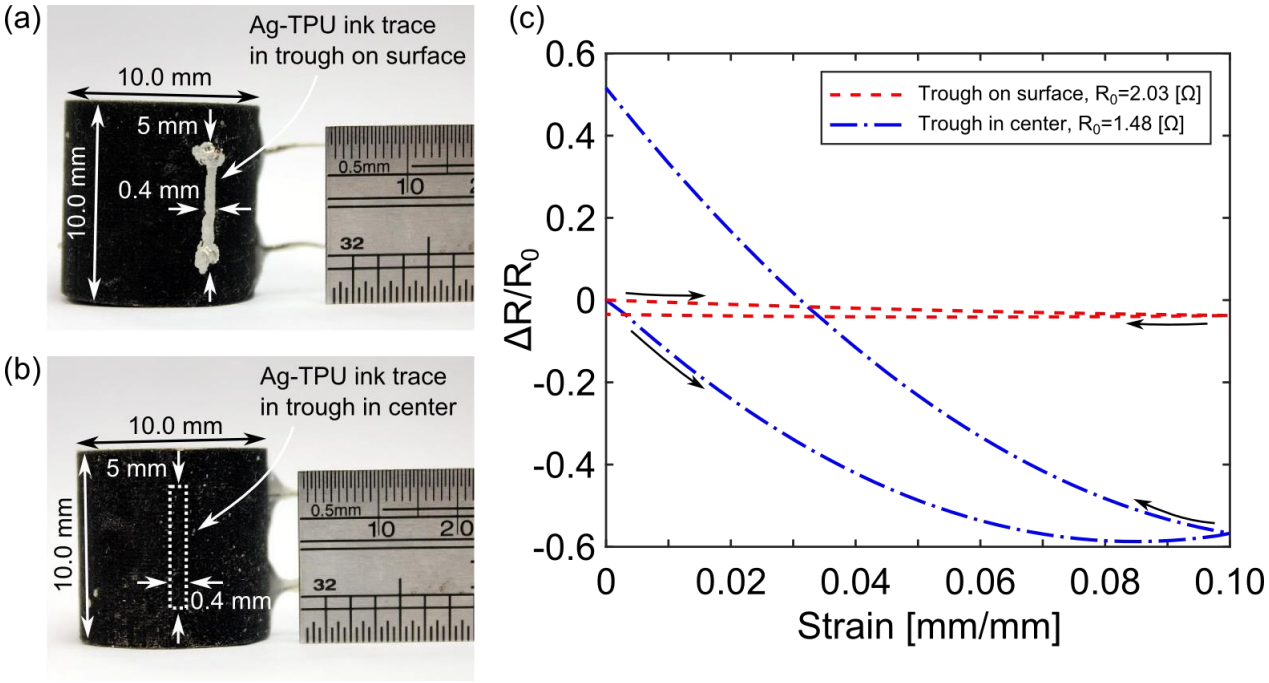

Figure S1. The role of the ink trace trough in determining resistance response is evaluated with cylindrical specimens that contain the trough (a) on their surface and (b) in their center, with (c) their corresponding resistance response. Arrows indicate loading and unloading portions of the measurements.

2 Evaluation of the vertical beam member of strain-sensitive specimen

To evaluate the influence of the vertical, buckling beam member of the strain-sensitive specimen on the change of resistance when specimens are subjected to uniaxial strain, a comparative benchmark specimen is fabricated. The benchmark is a solid specimen of the same overall dimensions as the strain-sensitive specimen. The strain-sensitive specimen and its solid counterpart are shown in Fig. S2(a) and (b), respectively. The strain-sensitive and the solid benchmark specimens are printed in the same build orientation to ensure that anisotropy associated with the 3D printing process are not influential in the comparison of measurements.

For a compressive displacement of 1.0 mm peak at a rate of 3 mm/min in the load frame, the normalized changes in resistance of the conductive ink trace paths are shown in Fig. S2(c). The results reveal that the strain-sensitive specimen experiences significant relative change in resistance when compared to the benchmark solid specimen. For instance, the strain-sensitive specimen has a relative change of resistance of 5.6% for an engineering strain of 3.9% that compares to the relative resistance change of 0.15% for the benchmark solid specimen for the same strain. Therefore, the particular geometry of the strain-sensitive specimen that triggers the elastic buckling response of the vertical beam member is crucial to the strain-sensing capability of the conductive ink trace, as described in the main text.

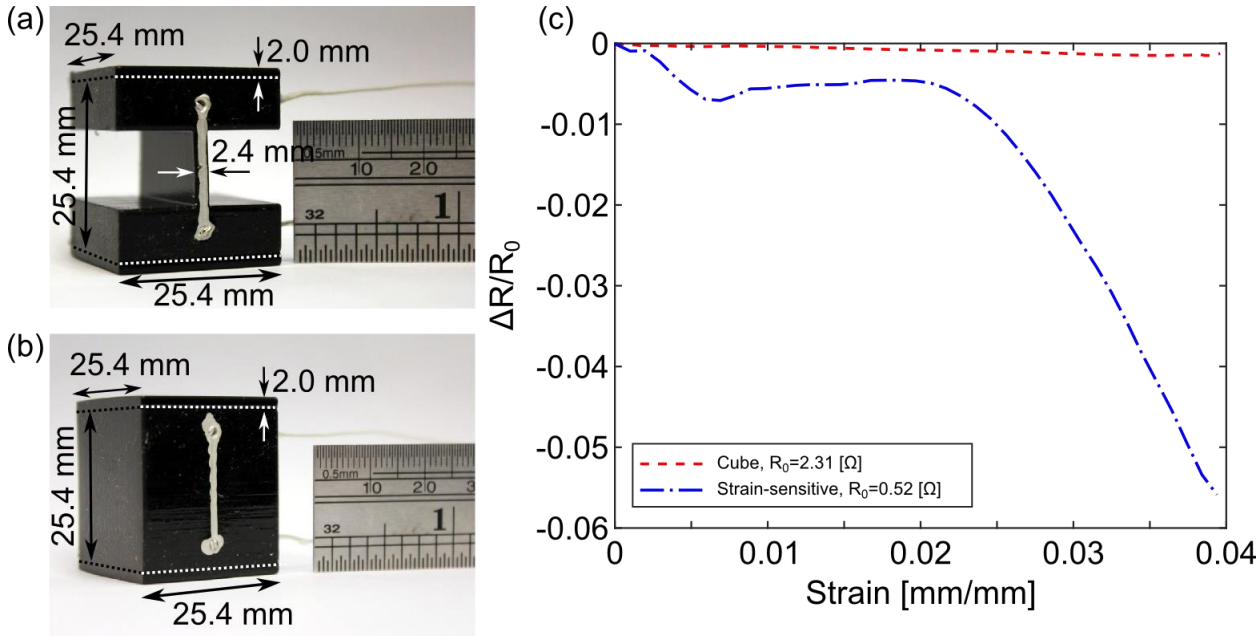

Figure S2. The influence of the vertical buckling beam member in (a) the strain-sensitive specimen is investigated using (b) an equivalent specimen without material removal with (c) corresponding resistance responses.